Silicon-Micromachined Wideband Sub-THz Frequency-Diverse Antenna

Mohammad-Reza Seidi, *Student Member, IEEE,* Mohammad Mehrabi Gohari, *Student Member, IEEE,* Alireza Madannejad, *Student Member, IEEE,* Umer Shah, *Senior Member, IEEE,* Joachim Oberhammer, *Senior Member, IEEE,*

Abstract—This paper presents the first compact, wideband, silicon-micromachined frequency-diverse antenna, operating across the 220-330 GHz range, designed explicitly for sub-THz imaging applications. The antenna consists of 80 slot radiating elements of twelve distinct sizes corresponding to half of the uniformly sampled wavelengths within the operating bandwidth. These elements are arranged in a Mills-Cross configuration for antenna designs A and B, supported by an innovatively shaped air-filled cavity. The cavity is engineered to support multiple higher-order, high-Q resonance modes, generating highly frequency-diverse, pseudo-random radiation patterns. The frequency-diverse antenna is fed by a three-section impedance-matching transitional direct waveguide and is fabricated using advanced silicon micromachining technology. This paper comprehensively analyzes the antenna's radiation patterns and impedance matching across the entire waveguide band. The compact prototype, with an overall size of 18 mm × 16 mm × 0.933 mm (effective antenna dimensions of $11\lambda \times 11\lambda \times 0.85\lambda$), is the most compact air-filled, cavity-backed frequency-diverse antenna reported to date. It demonstrates high radiation efficiency and is designed for direct mounting on a standard WR-3.4 waveguide flange. The antenna achieves a fractional bandwidth of 34%, with a return loss better than 10 dB, extending to 40% with a return loss better than 5 dB.

Index Terms—Sub-THz, wideband antenna, frequency-diverse antenna, Cavity-backed antenna.

I. INTRODUCTION

MICROWAVE imaging excels in its non-invasive penetration capability through optically opaque materials, which, in contrast to optical methods, allow the extraction of information from obscured objects, and has the ability to discriminate low-density materials. These properties make this technology indispensable in non-destructive testing, security, structural monitoring, and medical-imaging applications [1]–[4].

Microwave imaging systems suffer from high hardware complexity and slow data acquisition due to requiring numerous measurements in the typical array configurations, which limits their real-time performance [1]. To address these limitations, frequency-diverse

cavity-backed antennas have emerged as a solution for short-range imaging applications that feature faster measurement rates since no hardware reconfiguration or physical antenna scanning is needed. This antenna configuration significantly reduces hardware complexity, simplifies system design, and lowers cost and maintenance requirements, all while maintaining high resolution [5]–[7].

Unlike traditional narrow-beam steering antennas, the cavity-backed frequency-diverse antenna intentionally generates pseudo-random radiation patterns. By varying the frequency, these radiation patterns change, offering a diverse range of patterns. The goal is to generate as many independent radiation patterns as possible across different frequencies, maximizing the antenna's effectiveness for imaging applications. The unique cavity-backed configuration of these antennas significantly enhances their frequency-diversity capability, which is required for image reconstruction [8]–[12]. A cavity-backed frequency-diverse antenna system with wideband performance, generates a frequency-diverse resonance pattern that effectively illuminates the field of view with frequency-diverse radiation patterns, and creates a large physical aperture. Its simplicity, requiring only a simple feeding and no reconfigurable elements, enables uncomplicated implementation, in contrast to, for instance, phased-array systems requiring phase shifters or a mechanical scanning system requiring mechanical reconfigurability [1], [6], [13].

In [14], the Mills-Cross configuration was proposed as the optimal arrangement for transmission Tx and reception Rx antennas, offering the highest necessary k-space coverage for imaging by utilizing slot radiators.

Previous works [15], [16] have proposed frequency-diverse antennas for computational imaging at W-band frequencies. Zvolensky et al. [15] introduced a W-band sparse imaging system that utilizes frequency-diverse cavity-fed metasurface antennas, where a high-Q cavity geometry supports multiple distinct higher-order modes. On the other hand, Zhao et al. [16] proposed a frequency-polarization-port-diverse (FPPD) cavity imager at W-band, focusing on bunching random beams. This design uses elliptical holes and a dual-polarized horn antenna to generate radiation patterns across frequencies and polarization states.

The long wavelengths of microwave frequencies limit the resolution and result in large sensor hardware. Therefore, sub-THz frequencies, due to their shorter wavelengths, have
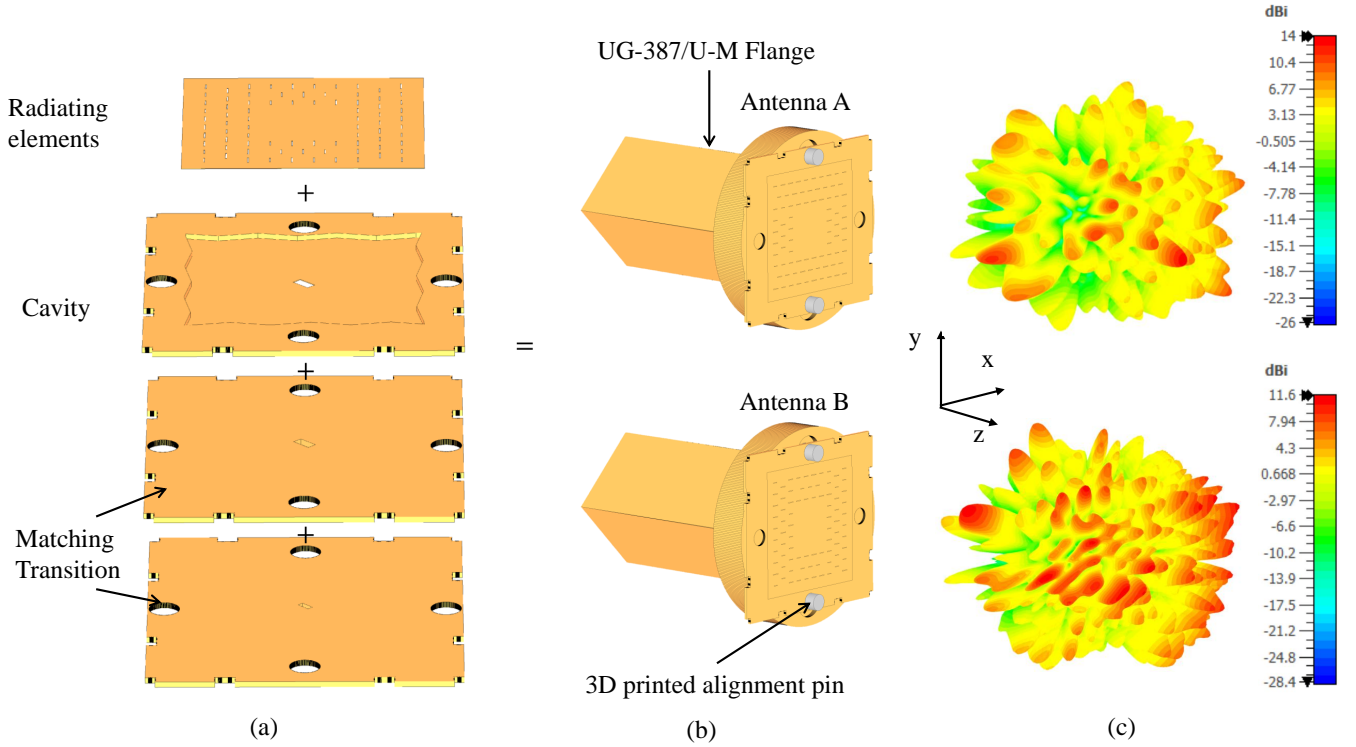
Fig. 1. Operating principle of the proposed air-filled cavity-backed frequency diverse sub-THz antenna. (a) matching transition, cavity, and radiating elements 3D view. (b) The Schematic view of the two proposed Antenna pairs A and B. (c) 3D view of simulated radiation patterns of antennas A and B at 240 GHz.

been receiving much attention to enhance the imaging resolutions and to shrink the antenna size [17]–[23].

At sub-THz frequencies, [24] introduces a frequency-diverse antenna designed for terahertz communication systems, integrating an oversized metallic cavity with metallic scatterers and a 3D-printed dielectric lens. The antenna has dimensions of 45 mm × 45 mm × 15 mm. It operates in the 220 to 330 GHz range, generating quasi-random radiation patterns over a wide frequency band. The random orientation of scatterers inside the cavity and using a cyclic olefin copolymer (COC) lens with varying pillar heights enhance the diversity and directivity of the antenna's radiation patterns.

A pivotal advancement in sub-THz technology has been the development of silicon-micromachining fabrication techniques, in particular, deep reactive ion etching (DRIE), which facilitates the creation of very small and accurate features, as well as nanometer surface roughness critical for low losses of rectangular-waveguide based sub-THz components [25]–[28]. This is particularly important at higher frequencies, where tightly controlled feature sizes and tolerances are necessary to meet the requirements of geometrical tolerances for maintaining excellent electromagnetic properties. Furthermore, as compared to conventional manufacturing methods such as CNC milling, silicon micromachining is volume manufacturable, cost-effective for mass production, and has a high product uniformity [29]–[31].

Also, as it enables the integration of multiple functions onto a single silicon chip, it significantly reduces the size and weight of a front-end system, which is advantageous for applications where size and weight are critical [32]–[35].

The range and cross-range resolution of a radar sensor are the key performance indicators of the system to discriminate objects in close proximity, both in distance and angle. The range (distance) resolution is given by the following relation [36]:

$$\Delta R = \frac{c_0}{2BW} \tag{1}$$

where c_0 represents the speed of light in free space, and BW denotes the available measurement bandwidth.

The cross-range (angular) resolution is given by [36]:

$$\Delta\theta = \frac{\lambda}{D} \tag{2}$$

where λ is the wavelength at the operating frequency, and D represents the dimension of the aperture of the antenna system. Sub-THz frequencies provide access to large bandwidth, enhancing the range resolution, and the millimeter-sized wavelengths of sub-THz frequencies make it feasible to utilize a relatively large physical aperture as compared to the wavelength, which also provides high angular resolution.

This paper presents the first wideband, compact, air-filled cavity-backed, frequency-diverse antenna, utilizing a direct waveguide feeding method, and fabricated using silicon
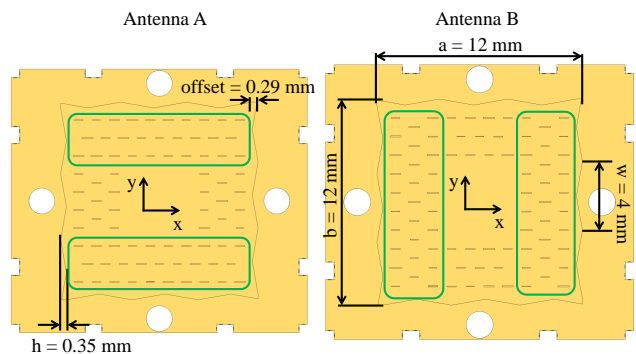
Fig. 2. Interior view of the antenna A and B backing cavity featuring asymmetric sawtooth boundaries. The green boundary highlights the difference in spatial positions of the radiating elements.
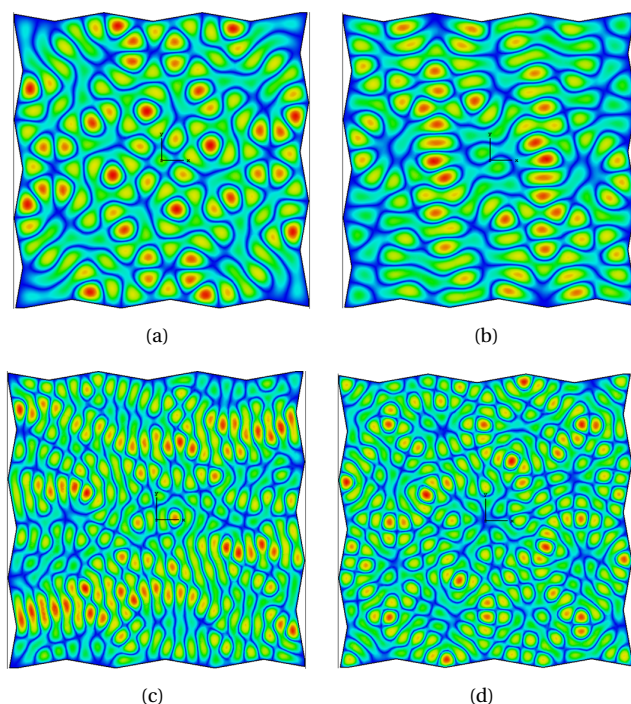

Fig. 3. Electric field distribution of four resonance modes of the cavity: (a) $f = 220.854$ GHz, (b) $f = 221.297$ GHz, (c) $f = 328.839$ GHz, (d) $f = 328.892$ GHz.

micromachining for operation in the 220-330 GHz range. The antenna is designed explicitly for sub-THz imaging systems and is the most compact air-filled cavity-backed, frequency-diverse antenna reported to date. This work comprehensively examines the antenna's design, analysis, and performance evaluation, with all simulations and optimizations conducted using CST Studio.

II. CAVITY-BACKED FREQUENCY-DIVERSE ANTENNA DESIGN

The proposed antenna is conceptually illustrated in Fig. 1. The design incorporates a matching transition from a standard WR-3.4 waveguide interface, leading to the air-filled resonant cavity with nonuniform borders, which is topped by a radiating slot element. The antenna's radiation pattern is intentionally designed to produce a pseudo-random distribution, as illustrated. The antenna is applicable in short-range imaging, and a high-gain antenna is not required.

The frequency-diverse antenna is composed of the following components, which are described in the following subsections:
(A) Air-filled resonant cavity,
(B) Radiating elements,
(C) Input transition.

A. Air-Filled Resonant Cavity Design

The interior geometry and dimensions of the cavity are illustrated in Fig. 2. The sidewalls of the cavity measure 12 mm, approximately $11\lambda_c \times 11\lambda_c$, with a cavity height of 278 µm. Unlike the design presented in [15], the unique sawtooth boundaries on all four sidewalls are specifically engineered to excite the different populations of radiating elements. These sawtooth boundaries facilitate the excitation of nonuniform higher-order modes, resulting in varied amplitude and phase distributions of the electric field across different cavity segments.

The dimensions of the size of the sawtooth boundary and offset are designed to create maximum nonuniform resonances. Different dimensions can be designed based

on the radiating elements and their position. Using the Eigenmode solver in CST Studio, simulations revealed a rich spectrum of 277 distinct modes across the desired bandwidth, as illustrated in Fig. 3. Notably, even a slight frequency shift of $\Delta f = 0.443$ GHz at 220 GHz and a 0.053 GHz frequency shift at 329 GHz result in distinct resonances, as demonstrated in Figs. 3(a)-(d).

B. Radiating Elements

Slot radiators were selected for their simplicity and resonance characteristics, with a typical fractional bandwidth of around 5-10%, allowing for efficient operational bandwidth coverage. Unlike the approach in [15], which uses single-size slots, varying the individual slot lengths to match the cavity's resonances enhances the generation of diverse and independent radiation patterns.

Twelve frequencies ranging from 220 to 320 GHz were uniformly selected to cover the entire operational bandwidth. The lengths of the slots were then determined to be half of the corresponding wavelengths at these frequencies.

The spatial arrangement of the slots is important to the performance of the radiating elements. The center of the radiators on the cavity's cap cannot accommodate slots, as the feed of the cavity (discussed later in this section) is positioned below it.

Utilizing the Mills-Cross configuration, the primary slots are aligned horizontally for antenna design A, as shown in Fig. 2, and vertically for antenna design B. A random distribution process was employed for the spatial

arrangement of the slots to achieve higher diversity in pseudo-random radiation patterns.

This approach resulted in the configuration of 80 radiating slots, independently selected for both antenna A and B, ensuring a comprehensive and varied set of radiation patterns that effectively span the k-space [5].

The periodicity of the radiation slots' arrangement was set to the guide wavelength at the center frequency of 275 GHz (1.1 mm), with each slot's width established as one-tenth of its corresponding length. The thickness of the radiating elements was determined by fabrication/material constraints to 30 µm.
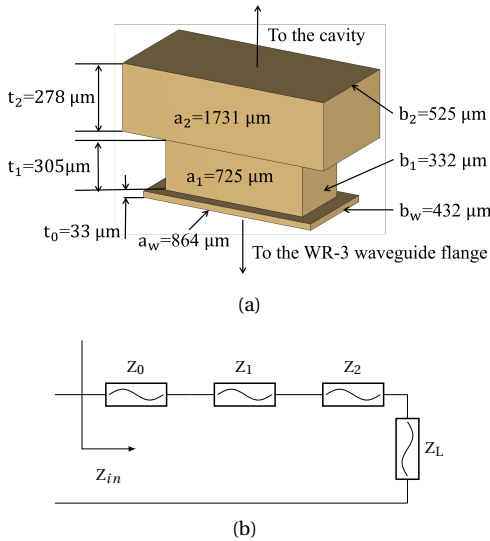
Fig. 4. (a) Overall view of the cavity with the direct feed. (b) General matching circuit model.

C. Input Transition

A waveguide transition enables the transition from the input waveguide flange to the cavity. Figure 4(a) visualized the input transition configuration shown in Fig. 1(a) to show the optimized dimensions. The two upper waveguide sections are designed for impedance matching between the standard WR-3.4 waveguide and the cavity. The bottom section, with dimensions equivalent to the standard waveguide flange (864µm × 432µm), serves as an interface with the input waveguide flange. The thickness of each section of the matching transition is dictated by the available standard waver that comes later in the fabrication section. An optimization procedure was conducted utilizing CST Studio on the dimensions of the waveguide sections, a_i and b_i, to achieve sufficient return loss throughout the 220-330 GHz frequency range.

The corresponding circuit model is shown in Fig. 4(b), where the matching network comprises two frequency-dependent impedances, Z_1 and Z_2. The bottom section of the transition, Z_0, has the impedance of a standard WR-3.4 waveguide, and the impedance Z_L represents the input impedance of the air-filled cavity and radiation slots.

As shown in Fig. 1, mounting the antennas on the standard flange requires the use of alignment pins. To avoid interference between the alignment pins and the cavity—which degrades the number of cavity resonances and conflicts with the location of the slot radiators—the feed structure is rotated by 45° in-plane.

III. FABRICATION

The silicon-micromachining fabrication process for the sub-THz frequency diverse antenna involves several steps to achieve the desired fabrication properties. The process is illustrated in Fig. 5 and utilizes so-called silicon-on-insulator (SOI) wafers, consisting of a device layer of 30 µm and a handle layer of 275 µm. The latter forms the structural base of the cavity, and the former is the layer into which the radiating slots are etched. A buried oxide (BOX) layer of 3 µm in between these two layers isolates the device layer from the handle layer. It acts as an etch stop to etch these two layers with different geometrical features independently. The final antennas are composed by vertically assembling three chips of these SOI wafers, resulting in a total of six individually etched layers.

The sequence of fabrication steps is as follows:

1) **Hard mask disposition:** A 2 µm thick silicon dioxide layer is grown on both sides of the SOI wafer. This layer serves as a hard mask for the subsequent deep-silicon etching process.

2) **Photolithography:** Positive photoresist is applied to one side of the wafer, and the pattern of the cavity and radiating elements is transferred via exposure. The oxide layer on this side is then etched to form the hard mask. The process is repeated for the other side of the wafer.

3) **Deep Reactive Ion Etching (DRIE):** Utilizing the BOSCH process, DRIE is performed to etch through the silicon layers down to the BOX layer, creating the cavities and slots as defined by the hard masks.

4) **Oxide etching:** The surface oxides (including the BOX and hard masks) are removed in this step to yield a smooth silicon surface.

5) **Metallization:** All chips are first coated with a 50 nm-thick titanium tungsten adhesion layer. A gold layer is then deposited on the chips using a sputtering technique, resulting in a 1.5 µm gold layer, which provides effective conductive surfaces, which is essential for high radiation efficiency, minimized losses, and high-Q resonances for high frequency diversity.

6) **Assembly:** The device is constructed of three layers, which are aligned and bonded using a thermo-compression bonding method [37].

High-resolution Scanning Electron Microscope (SEM) images of the cavity, along with two differently sized slots with lengths of 525 µm and 550.4 µm, and widths of 55.6 µm and 53.9 µm, are shown in Fig. 6.

Optical microscope pictures of the fabricated cavity with radiating elements in both antenna A and antenna B arrangements are displayed in Fig. 7.
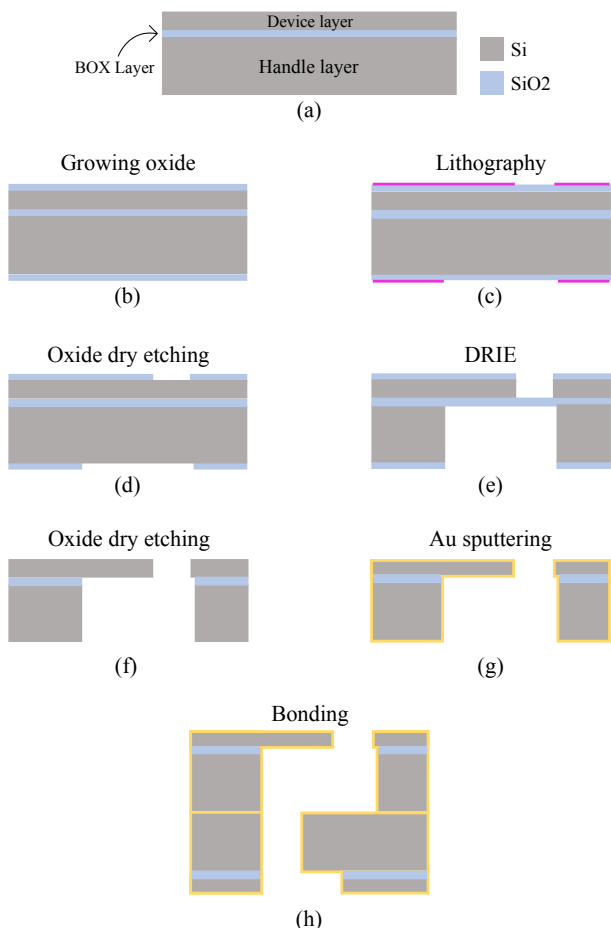
Fig. 5. Fabrication fellow process: (a) cross-section view of an SOI wafer; (b) oxide growing on both sides; (c) lithography; (d) hard mask; (e) silicon etching; (f) removing oxide layers; (g) metallization; (h) thermo-compression bonding.
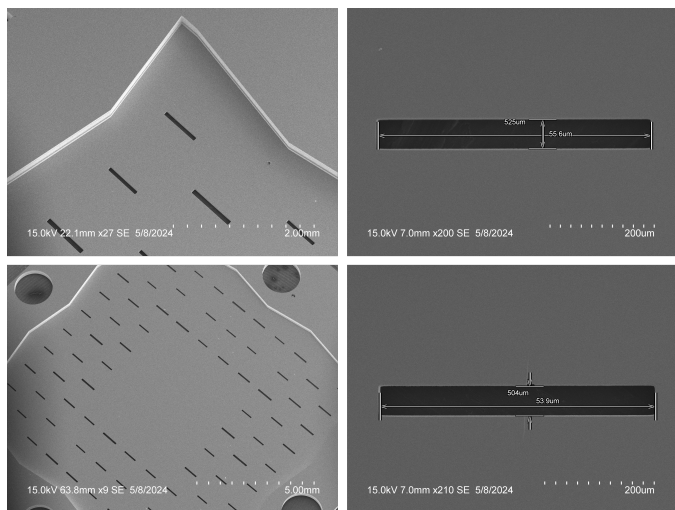

Fig. 6. SEM image of the fabricated cavity, showcasing an overall view of the cavity, sawtooth boundaries, and two radiating elements.
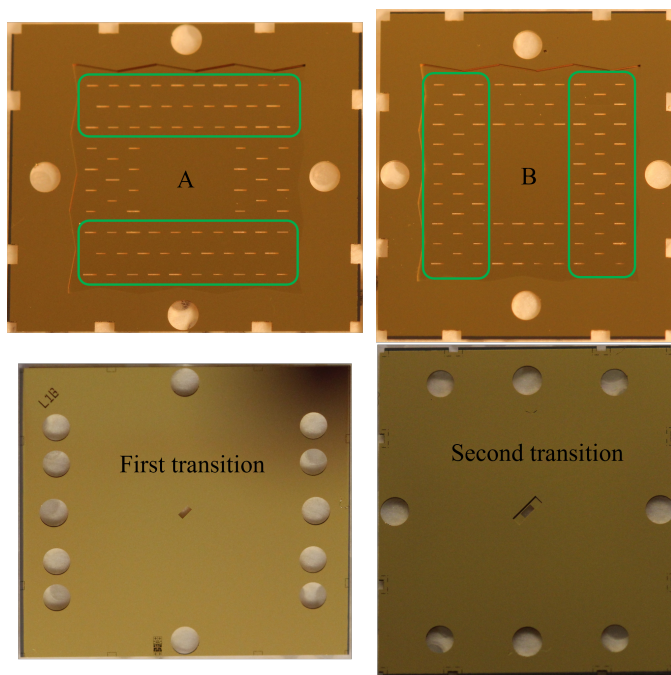

Fig. 7. Optical images of the fabricated cavity featuring radiating elements configured for antennas A and B and the transition layers.

The high Q-factor modes necessary for distinct cavity modes at closely spaced frequencies are ensured by the low surface roughness in the order of a few nanometers of the cavity boundaries, which is a specific strength of silicon micromachining compared to other fabrication techniques.

IV. MEASUREMENTS

The measurements are performed in an anechoic antenna measurement chamber operable within 67-750 GHz [22]. The chamber is equipped with a 4-degree-of-freedom fully automated robot and is covered with high-frequency absorbers to minimize reflections, facilitating accurate radiation pattern measurements. The S-parameters and patterns are measured using a Rohde & Schwarz ZVA-24 Vector Network Analyzer (VNA) with ZC-330 frequency extenders operating in the 220-330 GHz. The measurement setup is calibrated with a standard calibration kit using the Through-Offset-Short-Match (TOSM) method, shifting the measurement reference planes to the surface of the waveguide flanges right at the input port.

The measurement setup, depicted in Fig. 8, involves mounting the Antenna Under Test (AUT) on the standard WR-3.4 waveguide flange of a 220-330 GHz frequency extender.

The measured and simulated reflection coefficients, S_{11}, for antennas A and B are shown in Fig. 9. These results verify the impedance matching of both antennas. The slight discrepancies between the measured and simulated S_{11} values are attributed to misalignments in the impedance matching layer and fabrication tolerances.

As reported by our group in [38], the silicon micromachining losses are very low, better than 0.07
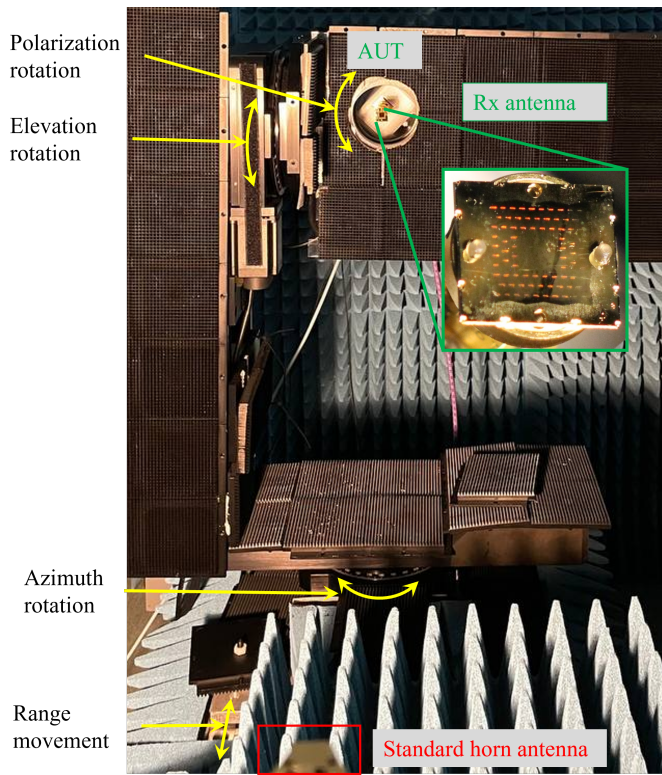
Fig. 8. Measurement pattern setup: The frequency-diverse antenna mounted on the automated robot with a 25 dBi gain standard horn antenna serving as the transmitter.

Fig. 9. The measured and simulated S_{11} for both antennas A and B over the frequency range of 220 GHz to 330 GHz.
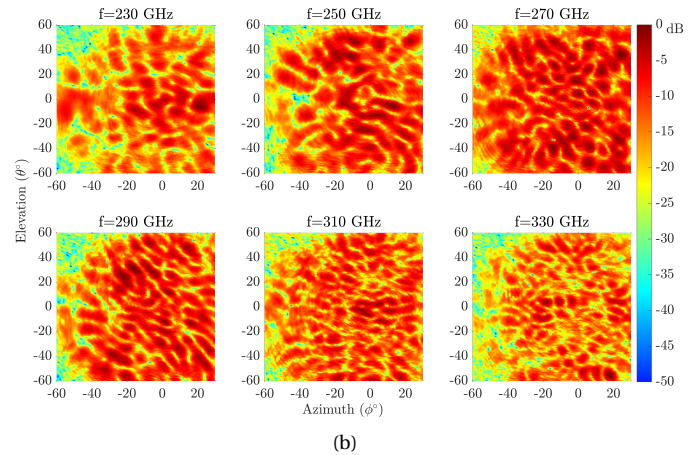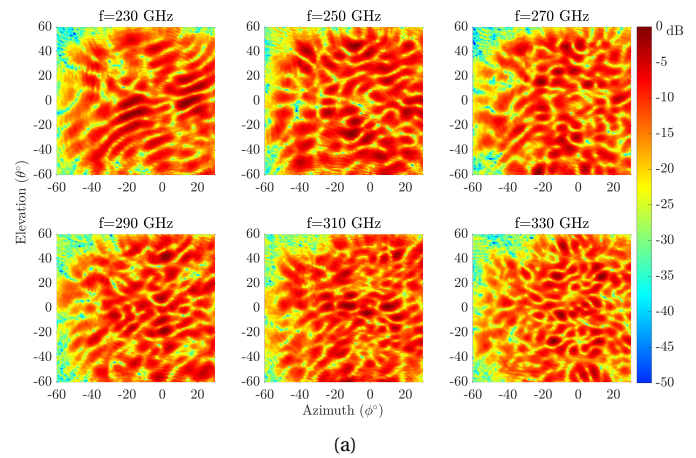

Fig. 10. (a) Measured patterns of the antenna A. (b) Measured patterns of antenna B under conditions similar to antenna B, illustrating the diversity and effectiveness of the design.
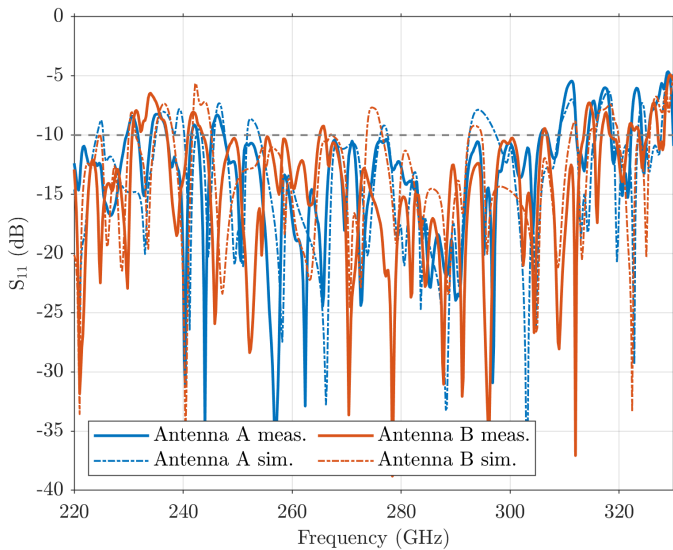
dB/mm, contributing minimally to any differences observed. The measured fractional bandwidth (FBW) is 34% for a return loss better than 10 dB and 40% for a return loss better than 5 dB, limited by the waveguide bandwidth of the measurement instrumentation. Both antennas A and B demonstrate excellent matching performance across the entire waveguide band.

Radiation pattern measurements were conducted in both azimuth and elevation, spanning a field of view of -60° to 30° (due to setup measurement restriction that a metalic arm of the robot limits the azimuth range) and ±60°, respectively, with a 1° step size across 551 frequencies, with each frequency step sized at 200 MHz. The antennas are positioned at a distance of 0.6 m to ensure far-filled illumination while maintaining sufficient dynamic range of the setup. A standard-gain horn antenna with 25dBi gain is employed as the transmitting antenna to measure radiation patterns for antennas A and B. The measured radiation patterns of the antennas A and B at six frequencies from 230 GHz to 320 GHz with 20 GHz frequency intervals are shown in Fig. 10.

The radiation patterns vary significantly across the frequency range, indicating the frequency-dependent behavior of the antennas. The variation in colors from red to blue represents the power levels in dB, with red indicating the highest power and blue indicating the lowest.

These frequency-dependent radiation patterns are important for evaluating and optimizing the performance of the frequency-diverse antenna system in imaging and communication applications at sub-THz frequencies.
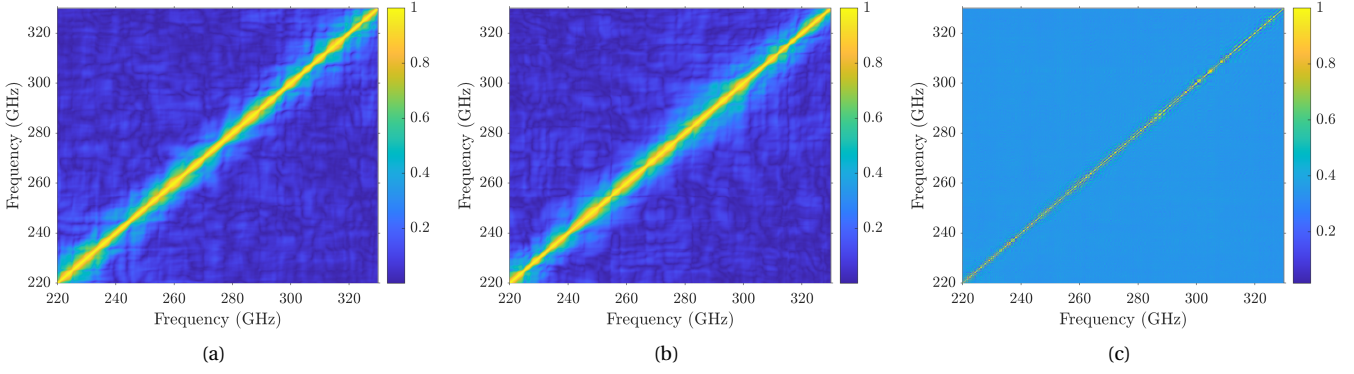
Fig. 11. Pattern independency graphs for antennas (a) A, (b) B, and (c) combination of antennas A and B.

V. DISCUSSION

The antenna setup has 110 GHz bandwidth, resulting theoretically in a range resolution of better than 1.4 mm as calculated from (1). A figure of merit called pattern independence was defined to evaluate the effectiveness of the generated diverse patterns. This metric qualitatively assesses how different scene parts are independently illuminated at various frequencies. Patterns that illuminate the same parts of the scene do not contribute additional information:

$$I(m,n) = \frac{\sum^i \sum^j U(f_m, \theta_i, \phi_j) \times U^*(f_n, \theta_i, \phi_j)}{\|U(f_m, \theta, \phi)\|_2 \times \|U(f_n, \theta, \phi)\|_2} \quad (3)$$

where $U(f, \theta, \phi)$ is the measured pattern at frequency f and angles θ and ϕ, and $\|.\|_2$ denotes the Euclidean norm (or 2-norm). Ideally, if the patterns are orthogonal, the independence matrix will be an identity matrix.

Fig. 11 illustrates the frequency pattern dependence of the Mills-Cross antenna configuration for antennas A and B and the combination of both. Fig. 11(a) shows the antenna A frequency pattern dependence, where the antenna A pattern varies by frequency between 220 GHz and 330 GHz. A clear diagonal trend indicates a consistent frequency-dependent variation in the transmitted radiation pattern.

Fig. 11(b) presents the antenna B frequency pattern dependence, where similar diagonal patterns are observed to exhibit frequency-dependent variations in its pattern across the same frequency range.

Fig. 11(c) shows the combined antennas A and B frequency pattern dependence, where the frequency variation patterns of both antennas are compounded. The combined antennas A and B frequency pattern dependence is calculated from 3. The. The combined radiation patterns are substituted as:

$$U_{AB}(f_m, \theta_i, \phi_j) = \sqrt{U_A(f_m, \theta_i, \phi_j) \times U_B(f_m, \theta_i, \phi_j)}.$$

Here, the diagonal pattern dependence becomes more concentrated, reflecting the combined response of both antennas over the entire frequency range. This demonstrates how the interaction between the antennas

A and B results in a consistent frequency response across the range of interest.

The calculated pattern independence applies both to the measured pattern's azimuth and elevation span—a broader azimuth and elevation span result in a narrower distribution of pattern independence.

In order to compare the achievements introduced in this work, TABLE I provides a summary of previous works compared to the current study, highlighting the essential approaches and findings. This work presents a compact frequency-diverse antenna operating in the 220-310 GHz range (with extension to 330 GHz), offering a fractional bandwidth of 34% (and up to 40%). Compared to previous designs, such as [24] with dimensions $41 \times 41 \times 13.63 \lambda_c^3$, this antenna is significantly smaller, with dimensions of only $11 \times 11 \times 0.85 \lambda_c^3$, making it one of the most compact designs at sub-THz frequencies. Despite its smaller size, the antenna achieves a return loss of ≤ -10 dB, comparable to the best-performing designs in the literature, while supporting wideband operation.

One key advantage of this work is using direct transition waveguide feed and slot radiators, which enhance pattern diversity while maintaining low return loss. The silicon micromachining fabrication process allows for more precise construction and easier integration into compact systems compared to conventional methods such as CNC milling or 3D printing, which are used in other works. This makes the design highly suitable for applications requiring compact, high-resolution radar and imaging systems at sub-THz frequencies.

VI. CONCLUSION

This paper addresses several challenges associated with antennas for short-range imaging systems, such as achieving a wideband frequency range while miniaturizing system size and reducing complexity. The silicon micromachined wideband sub-THz antenna combines innovative cavity-backed and frequency-diverse designs to optimize performance across 220-330 GHz. The unique design and implementation of radiating elements, alongside silicon micromachining, significantly enhance the antenna's operational efficiency and the quality of

TABLE I
COMPARISON OF THE FREQUENCY-DIVERSE PATTERN ANTENNA WITH PREVIOUS WORKS.

Ref.	Frequency (GHz)	FBW (%)	Size	S_{11} (dB)	Feed type	Radiating elements	Fabrication method
[5]	17.5-26.5	41	$7.33 \times 7.33 \lambda_c^2$	≤ -10	Coaxial	cELCs	PCB
[10]	17.5-26.5	41	$21 \times 21 \times 11.18 \lambda_c^3$	≤ -5	Coaxial	Holes	-
[11]	32-36	11.8	$(6.8)^2 \pi \times 2.27 \lambda_c^3$	≤ -10	Waveguide	Different elements	PCB & CNC milling
[6]	17.5-26.5	41	$14.7 \times 14.7 \times 3.9 \lambda_c^3$	≤ -8	Waveguide	Holes	3D printing
[14]	17.5-26.5	41	$7.35 \times 7.35 \lambda_c^2$	≤ -10	Coaxial	Irises	PCB
[15]	75-110	37.8	$12.5 \times 12.5 \times 0.4 \lambda_c^3$	≤ -5	Waveguide	Slots	CNC milling
[16]	76-81	6.37	$(15.79)^2 \pi \times 1.78 \lambda_c^3$	≤ -5	Waveguide	Elliptical holes	3D printing & metal plating
[24]	220-330	40	$41 \times 41 \times 13.63 \lambda_c^3$	≤ -10	Waveguide	COC lens	3D printing
This work	**220-310 (220-330)**	**34 (40)**	$11 \times 11 \times 0.85 \lambda_c^3$	$\leq -10(-5)$	**Waveguide**	**Slots**	**Silicon micromachining**

the imaging results. Experimental validations within an anechoic chamber confirm the simulation expectations on the design, showcasing the antenna's ability to produce independent radiation patterns necessary for high-resolution imaging. The measurements highlight the antenna's frequency-diverse feature, validating its potential for integration into advanced imaging systems.

VII. ACKNOWLEDGMENT

REFERENCES

[1] D. Sheen, D. McMakin, and T. Hall, "Three-dimensional millimeter-wave imaging for concealed weapon detection," *IEEE Transactions on Microwave Theory and Techniques*, vol. 49, no. 9, pp. 1581–1592, 2001.

[2] G. Matrone, A. S. Savoia, G. Caliano, and G. Magenes, "The delay multiply and sum beamforming algorithm in ultrasound b-mode medical imaging," *IEEE Transactions on Medical Imaging*, vol. 34, no. 4, pp. 940–949, 2015.

[3] X. Zhuge and A. G. Yarovoy, "A sparse aperture mimo-sar-based uwb imaging system for concealed weapon detection," *IEEE Transactions on Geoscience and Remote Sensing*, vol. 49, no. 1, pp. 509–518, 2011.

[4] R. Peng, O. Yurduseven, T. Fromenteze, and D. R. Smith, "Advanced processing of 3d computational microwave polarimetry using a near-field frequency-diverse antenna," *IEEE Access*, vol. 8, pp. 166261–166272, 2020.

[5] O. Yurduseven, J. N. Gollub, A. Rose, D. L. Marks, and D. R. Smith, "Design and simulation of a frequency-diverse aperture for imaging of human-scale targets," *IEEE Access*, vol. 4, pp. 5436–5451, 2016.

[6] T. Fromenteze, O. Yurduseven, M. F. Imani, J. Gollub, C. Decroze, D. Carsenat, and D. R. Smith, "Computational imaging using a mode-mixing cavity at microwave frequencies," *Applied Physics Letters*, vol. 106, no. 19, p. 194104, 05 2015. [Online]. Available: https://doi.org/10.1063/1.4921081

[7] O. Yurduseven, M. F. Imani, H. Odabasi, J. Gollub, G. Lipworth, A. Rose, and D. Smith, "Resolution of the frequency diverse metamaterial aperture imager," *Progress In Electromagnetics Research*, vol. 150, pp. 97–107, 2015.

[8] M. F. Imani, J. N. Gollub, O. Yurduseven, A. V. Diebold, M. Boyarsky, T. Fromenteze, L. Pulido-Mancera, T. Sleasman, and D. R. Smith, "Review of metasurface antennas for computational microwave imaging," *IEEE Transactions on Antennas and Propagation*, vol. 68, no. 3, pp. 1860–1875, 2020.

[9] G. Lan, M. F. Imani, Z. Liu, J. Manjarrés, W. Hu, A. S. Lan, D. R. Smith, and M. Gorlatova, "Metasense: Boosting rf sensing accuracy using dynamic metasurface antenna," *IEEE Internet of Things Journal*, vol. 8, no. 18, pp. 14110–14126, 2021.

[10] T. Fromenteze, O. Yurduseven, M. Boyarsky, J. Gollub, D. L. Marks, and D. R. Smith, "Computational polarimetric microwave imaging," *Opt. Express*, vol. 25, no. 22, pp. 27488–27505, Oct 2017. [Online]. Available: https://opg.optica.org/oe/abstract.cfm?URI=oe-25-22-27488

[11] M. Zhao, S. Zhu, D. Li, T. Fromenteze, M. Khalily, X. Chen, V. Fusco, and O. Yurduseven, "Frequency-diverse bunching metasurface antenna for microwave computational imaging," *IEEE Transactions on Antennas and Propagation*, vol. 72, no. 5, pp. 3950–3961, 2024.

[12] M. Zhao, S. Zhu, D. Hu, H. Huang, X. Chen, C. Guo, J. Chen, and A. Zhang, "3-d printing disordered-cavity-based metaimager for coincidence imaging," *IEEE Microwave and Wireless Components Letters*, vol. 31, no. 6, pp. 620–623, 2021.

[13] T. A. Sleasman, M. F. Imani, A. V. Diebold, M. Boyarsky, K. P. Trofatter, and D. R. Smith, "Implementation and characterization of a two-dimensional printed circuit dynamic metasurface aperture for computational microwave imaging," *IEEE Transactions on Antennas and Propagation*, vol. 69, no. 4, pp. 2151–2164, 2021.

[14] O. Yurduseven, J. N. Gollub, D. L. Marks, and D. R. Smith, "Frequency-diverse microwave imaging using planar mills-cross cavity apertures," *Opt. Express*, vol. 24, no. 8, pp. 8907–8925, Apr 2016. [Online]. Available: https://opg.optica.org/oe/abstract.cfm?URI=oe-24-8-8907

[15] T. Zvolensky, V. R. Gowda, J. Gollub, D. L. Marks, and D. R. Smith, "W-band sparse imaging system using frequency diverse cavity-fed metasurface antennas," *IEEE Access*, vol. 6, pp. 73659–73668, 2018.

[16] M. Zhao, S. Zhu, H. Huang, D. Hu, X. Chen, J. Chen, and A. Zhang, "W-band frequency-polarization-port-diverse cavity imager with bunching random beams," *Journal of Physics D: Applied Physics*, vol. 54, no. 35, p. 355106, jun 2021. [Online]. Available: https://dx.doi.org/10.1088/1361-6463/ac0928

[17] K. B. Cooper, R. J. Dengler, N. Llombart, B. Thomas, G. Chattopadhyay, and P. H. Siegel, "Thz imaging radar for standoff personnel screening," *IEEE Transactions on Terahertz Science and Technology*, vol. 1, no. 1, pp. 169–182, 2011.

[18] A. Mostajeran, S. M. Naghavi, M. Emadi, S. Samala, B. P. Ginsburg, M. Aseeri, and E. Afshari, "A high-resolution 220-ghz ultra-wideband fully integrated isar imaging system," *IEEE Transactions on Microwave Theory and Techniques*, vol. 67, no. 1, pp. 429–442, 2019.

[19] K. B. Cooper, R. J. Dengler, N. Llombart, T. Bryllert, G. Chattopadhyay, E. Schlecht, J. Gill, C. Lee, A. Skalare, I. Mehdi, and P. H. Siegel, "Penetrating 3-d imaging at 4- and 25-m range using a submillimeter-wave radar," *IEEE Transactions on Microwave Theory and Techniques*, vol. 56, no. 12, pp. 2771–2778, 2008.

[20] Y. Shang, H. Yu, H. Fu, and W. M. Lim, "A 239–281 ghz cmos receiver with on-chip circular-polarized substrate integrated waveguide antenna for sub-terahertz imaging," *IEEE Transactions on Terahertz Science and Technology*, vol. 4, no. 6, pp. 686–695, 2014.

[21] A. Mostajeran, S. M. Naghavi, M. Emadi, S. Samala, B. P. Ginsburg, M. Aseeri, and E. Afshari, "A high-resolution 220-ghz ultra-wideband fully integrated isar imaging system," *IEEE Transactions on Microwave Theory and Techniques*, vol. 67, no. 1, pp. 429–442, 2019.

[22] A. Madannejad, M. M. Gohari, U. Shah, and J. Oberhammer, "High-gain circularly polarized 500–750 ghz lens antenna enabled by silicon micromachining," *IEEE Transactions on Antennas and Propagation*, vol. 72, no. 5, pp. 4077–4085, 2024.

[23] O. Glubokov, M. M. Gohari, J. Campion, and J. Oberhammer, "Compact w-band silicon-micromachined filters with increased

This article has been accepted for publication in IEEE Transactions on Terahertz Science and Technology. This is the author's version which has not been fully edited and content may change prior to final publication. Citation information: DOI 10.1109/TTHZ.2025.3528231

9

fabrication robustness," in *2022 IEEE/MTT-S International Microwave Symposium-IMS 2022*.   IEEE, 2022, pp. 329–332.

[24] M. S. Li, M. Abdullah, J. He, K. Wang, C. Fumeaux, and W. Withayachumnankul, "Frequency-diverse antenna with convolutional neural networks for direction-of-arrival estimation in terahertz communications," *IEEE Transactions on Terahertz Science and Technology*, vol. 14, no. 3, pp. 354–363, 2024.

[25] A. Karimi, U. Shah, A. Madannejad, and J. Oberhammer, "Silicon-micromachined subterahertz frequency beam-steered dual-port array antenna," *IEEE Transactions on Terahertz Science and Technology*, vol. 14, no. 2, pp. 258–268, 2024.

[26] K. Sarabandi, A. Jam, M. Vahidpour, and J. East, "A novel frequency beam-steering antenna array for submillimeter-wave applications," *IEEE Transactions on Terahertz Science and Technology*, vol. 8, no. 6, pp. 654–665, 2018.

[27] A. Gomez-Torrent, M. García-Vigueras, L. Le Coq, A. Mahmoud, M. Ettorre, R. Sauleau, and J. Oberhammer, "A low-profile and high-gain frequency beam steering subterahertz antenna enabled by silicon micromachining," *IEEE Transactions on Antennas and Propagation*, vol. 68, no. 2, pp. 672–682, 2020.

[28] M.-R. Seidi, A. Karimi, A. Madannejad, U. Shah, and J. Oberhammer, "Experimental validation of a notch-beam and frequency-scanning sub-thz radar," *IEEE Transactions on Terahertz Science and Technology*, pp. 1–10, 2024.

[29] H. Lu, S. Zhu, T. Skaik, B. Nie, Y. Liu, and Y. Wang, "Sub-terahertz metallic multibeam antenna based on a sliding aperture technique," *IEEE Transactions on Antennas and Propagation*, vol. 72, no. 1, pp. 290–299, 2024.

[30] G.-L. Huang, S.-G. Zhou, and T.-H. Chio, "Highly-efficient self-compact monopulse antenna system with integrated comparator network for rf industrial applications," *IEEE Transactions on Industrial Electronics*, vol. 64, no. 1, pp. 674–681, 2017.

[31] A. Vosoogh, A. Haddadi, A. U. Zaman, J. Yang, H. Zirath, and A. A. Kishk, "w-band low-profile monopulse slot array antenna based on gap waveguide corporate-feed network," *IEEE Transactions on Antennas and Propagation*, vol. 66, no. 12, pp. 6997–7009, 2018.

[32] A. Karimi, U. Shah, A. Madannejad, and J. Oberhammer, "Silicon-micromachined subterahertz frequency beam-steered dual-port array antenna," *IEEE Transactions on Terahertz Science and Technology*, vol. 14, no. 2, pp. 258–268, 2024.

[33] S. S. Yao, Y. J. Cheng, Y. F. Wu, and Y. Fan, "Isolation enhancement for w-band coplanar array antennas based on silicon micromachining technology," *IEEE Antennas and Wireless Propagation Letters*, vol. 19, no. 10, pp. 1744–1748, 2020.

[34] L. Liang, Y. Zhao, Y. Hu, Y. Xiao, H. Sun, and Z. Chen, "A broadband antenna design for integrated phased array using bulk silicon micromachining process," in *2023 IEEE 11th Asia-Pacific Conference on Antennas and Propagation (APCAP)*, vol. volume1, 2023, pp. 1–2.

[35] P. Liu, Y. Li, S. Wang, and Z. Zhang, "Millimeter-wave planar antenna array based on modified bulk silicon micromachining technology," *IEEE Transactions on Antennas and Propagation*, vol. 68, no. 11, pp. 7676–7681, 2020.

[36] M. Soumekh, *Synthetic Aperture Radar Signal Processing with MATLAB Algorithms*.   Wiley, 1999.

[37] M. Mehrabi Gohari, O. Glubokov, S. Yu, and J. Oberhammer, "On-chip integration of orthogonal subsystems enabled by broadband twist at 220–325 ghz," *IEEE Transactions on Microwave Theory and Techniques*, vol. 71, no. 9, pp. 3929–3936, 2023.

[38] B. Beuerle, J. Campion, U. Shah, and J. Oberhammer, "A very low loss 220–325 ghz silicon micromachined waveguide technology," *IEEE Transactions on Terahertz Science and Technology*, vol. 8, no. 2, pp. 248–250, 2018.